



Dynamics of trailing vortices in the wake of a generic high-speed train



J.R. Bell ^{a,*}, D. Burton ^a, M.C. Thompson ^a, A.H. Herbst ^b, J. Sheridan ^a

^a Department of Mechanical and Aerospace Engineering, Monash University, Clayton, Victoria 3800, Australia

^b Centre of Competence for Aero- and Thermodynamics, Bombardier Transportation, Vasteras, Sweden

ARTICLE INFO

Article history:

Received 5 September 2015

Received in revised form

29 May 2016

Accepted 3 June 2016

Available online 17 June 2016

Keywords:

Streamwise vortices

Vortex dynamics

Vortex shedding

Crow instability

Unsteady wake

High-speed train

Slipstream

ABSTRACT

The three-dimensional dynamics of a pair of counter-rotating streamwise vortices that are present in the wake of an ICE3 high-speed train typical of modern, streamlined vehicles in operation, is investigated in a 1/10th-scale wind-tunnel experiment. Velocity mapping, frequency analysis, phase-averaging and proper orthogonal decomposition of data from high-frequency multi-hole dynamic pressure probes, two-dimensional total pressure arrays and one-dimensional multi-hole arrays was performed. Sinusoidal, antisymmetric motion of the pair of counter-rotating streamwise vortices in the wake is observed. These unsteady characteristics are proposed to be representative of full-scale operational high-speed trains, in spite of the experimental limitations: static floor, reduced model length and reduced Reynolds number. This conclusion is drawn from favourable comparisons with numerical literature, and the ability of the identified characteristics to explain phenomena established in full-scale and scaled moving-model experiments.

© 2016 Elsevier Ltd. All rights reserved.

1. Introduction

Modern high-speed trains (HSTs) have a unique geometry among ground-vehicles, having a streamlined nose and tail with no fixed separation points and slender (length \gg height), small aspect-ratio (width:height ratio ≈ 0.75) bodies. The wake of a modern HST is in general expected to be a complex, unsteady, three-dimensional structure consisting of shear layers, vortex shedding, separation and recirculation regions, and a pair of counter-rotating streamwise vortices (Morel, 1980; Weise et al., 2006; Muld et al., 2012; Bell et al., 2014). These vortices move downwards and outwards as they progress away from the vehicle due to mutual induction and interaction with the image vortices beneath the ground (Weise et al., 2006; Muld et al., 2012; Heine et al., 2013; Schulte-Werning et al., 2001; Yao et al., 2013; Bell et al., 2014). These coherent vortices consist of vorticity that is generated at the surface of the train, and result from the interaction between the flow around the sides of the train and the down-wash over the roof and tail.

The greatest slipstream velocities occur in the wake of a HST (Baker, 2010; Baker et al., 2012; Bell et al., 2014, 2015). Slipstream is the air flow induced by a vehicle's movement, which continues to be an important consideration for aerodynamic performance and safe operation. Such flows can be hazardous to waiting commuters at platforms and track-side workers (Pope, 2007) as well as track-side infrastructure, due to significant induced-pressure forces. Regulations are in place that limit the magnitude of slipstream velocities a HST can induce (European Rail Agency (ERA), 2008; CEN European Standard, 2009).

* Corresponding author.

E-mail address: james.bell@monash.edu (J.R. Bell).

The authors have previously identified the presence of a pair of streamwise counter-rotating vortices in the time-averaged wake as the cause of the peak slipstream velocities (Bell et al., 2014). The significance of these vortices to characterising the slipstream velocity of a HST has also been identified by other authors (Baker, 2010; Weise et al., 2006; Muld et al., 2012). The largest slipstream velocities are measured as the vortices move downwards and outwards beyond the passage of the train. The magnitude and location of the peak of instantaneous slipstream velocity in the wake has been shown to be inconsistent in numerical investigations (Muld et al., 2012; Pii et al., 2014; Hemida et al., 2014) and scaled moving-model experiments (Baker, 2010; Bell et al., 2015). Previous wind-tunnel experiments by the authors have indicated that this is caused by periodicity in the wake (Bell et al., 2015). Understanding the source of this high variation, and peak instantaneous slipstream velocities provides the potential for mitigating the slipstream risk of HSTs. Further, such insight could lead to improving the stability and drag of the vehicle as well as the comfort of passengers (Peters, 1983; Schetz, 2001).

Uncertainty exists over the existence of a coherent time-varying vortex pair in the wake of a HST. This was discussed by Bearman (1997) who provided evidence of the potentially large differences between the instantaneous and time-averaged wake of an automotive vehicle. It is possible that the vortex pair only become visible in results due to the necessary processing required for providing a time-averaged description of the near-wake. Heine et al. (2013) have performed a novel moving-model experiment, essentially firing a scaled HST model through a Particle Image Velocimetry (PIV) window. Their results showed some evidence of one streamwise vortex in the near-wake, proposed to be one of a pair established in the time-average wake, but existing in instantaneous flow, however this evidence was not conclusive.

The streamwise vortex pair in the wake of HSTs has been predicted to exhibit spanwise oscillations by a number of numerical researchers applying different methodologies and investigating various, albeit similarly modern, HST geometries. Delayed detached eddy simulations (DDES) of an Inter-City-Express 2 (ICE2) HST by Muld et al. (2012), using Proper Orthogonal Decomposition (POD) and Dynamic Mode Decomposition (DMD) identified a streamwise vortex pair as the dominant flow regime. This is in contrast to high level of separation dominated flow regime (Morel, 1980; Ahmed, 1983). The dominant modes showed spanwise oscillations of the vortices occurring at a non-dimensionalized frequency, based on the freestream velocity and hydraulic diameter, of $St_{HD} = 0.085$, which they proposed to be caused by vortex shedding. Schulte-Werning et al. (2003) identified similar features on the same HST geometry in their unsteady simulations. Surface streamlines showed the point of origin of a pair of vortices oscillating in the spanwise direction around the vehicle's tail at $St_{HD} = 0.14$. Numerical simulations using the Lattice Boltzman Method (LBM) by Pii et al. (2014) identified vortex shedding off the vehicles sides at a frequency based on the freestream velocity and body width of $St_w = 0.18$ developing in the underbody due to interaction with the bogies, before being released into the near-wake. The near-wake exhibited spanwise velocity and pressure fluctuations, however, the resulting dynamics of the vortex pair was not presented. Results from a scaled wind-tunnel experiment on an ICE2 HST (Bell et al., 2014) indicate a potential agreement with the unsteady numerical predictions, however, without confirmation of the flow structures responsible, although frequency and probability distribution analysis indicated periodicity at the location of the time-averaged vortex pair. Thus, experimental confirmation of the near-wake dynamics of a HST and the mechanism causing the oscillation have not been explicitly identified or explained.

The counter-rotating pair of streamwise vortices in a HST's wake are common to a number of analogous flows. Such vortices are found in generic automotive ground-vehicles as established by Ahmed (1983) and others (Vino et al., 2005; Krajnović and Davidson, 2005; Strachan et al., 2007) that also identified movement downwards and outwards from the symmetry plane. Unsteady features of automotive wakes have been found by a number of researchers experimentally and numerically (Lienhart and Pêgo, 2012; Vino et al., 2005). In addition to the time-averaged streamwise vortex pair in the wake of a 25° backlight angle Ahmed body, researchers have identified signs of predominantly 2D vortex shedding in the vertical centre plane. This occurs as the shear layers over the roof and under-body roll up, feeding the upper and lower recirculating regions, but also rolling up to form the periodically shed vortex structures (Wang et al., 2013; Vino et al., 2005). A similar unsteady flow mechanism has been described by Gilhome et al. (2001) for a notchback automotive geometry.

Alternating vortex shedding, commonly known as Kármán shedding, occurs as two separated shear layers are alternately entrained into large-scale vortices that grow and eventually shed from a body (Gerrard, 1966). In addition to existing in automotive wakes, this type of vortex shedding has been identified at Reynolds numbers of $50 - 1 \times 10^7$, behind generic bodies such as two-dimensional cylinders (Tombazis and Bearman, 1997; Roshko, 1961; Williamson, 1996). The Kármán wake is due to a global instability, due to a region of local absolute instability that affects the entire flow. In contrast, the unsteady separating shear-layers are locally convectively unstable acting as amplifiers for disturbances as they advect downstream (Huerre and Monkewitz, 1990). The streamlined, highly 3D geometry of a HST tail presents a very different geometry for trailing-edge vortex shedding to automotive and even cylindrical bodies. Despite this, signs of shear-layer separation at the sides and the tail tip of a scaled model Inter-City-Express 3 (ICE3) HST have been identified (Bell et al., 2016), suggesting that vortex shedding still occurs even in this case.

Some researchers have identified unsteadiness of streamwise vortex pairs in automotive vehicle wakes. In a scaled wind-tunnel experiment, Sims-Williams et al. (2001) determined that the unsteady wake of a Rover 200 automotive vehicle, using a reconstruction technique from point measurements (Sims-Williams and Duncan, 1999), had two periodic features: the strengthening and the weakening of the pair of vortices together at a frequency based on the freestream velocity and square root of the frontal area of $St_{\sqrt{FA}} = 0.31$, and an alternating, asymmetric mode of strengthening/weakening of the vortex pair at $St_{\sqrt{FA}} = 0.10$. This experiment and analysis was also performed with a 25° backlight Ahmed body (Sims-Williams and Duncan, 2003), however, only the symmetric oscillation in strength and position of the vortex pair at a $St_{\sqrt{FA}} = 0.51$ was identified. This was attributed to vortex shedding from the bottom of the model base. Kohri et al. (2014) specifically investigated the dynamics of the pair of trailing vortices in the wake of the 27.5° backlight Ahmed body in scaled wind-tunnel

experiments. Hot-wire data identified a quasi-periodic motion, 180° out-of-phase, of the vortex pair at a $St_{\sqrt{FA}} = 0.1$. Short-averaged PIV vorticity fields associated this to the alternating growth and decay of each of the vortices. Hot-wire measurements also showed a dominant frequency of $St_{\sqrt{FA}} = 0.5$ in both the downwash and upwash regions in the longitudinal plane, yet with no correlation between the two. A degree of correlation was found between the downwash and one of the streamwise vortices.

An alternative, seemingly analogous flow is the trailing pair of vortices that develops from the wingtips of modern aircraft (Breitsamter, 2011; Spalart, 1998). Idealized aerodynamic theory associates this pair with the merging of a number of smaller longitudinal vortices, similar to that proposed by Sims-Williams et al. (2006) for an Ahmed body. This counter-rotating vortex pair exhibits the ‘Crow instability’ (Crow, 1970) that develops due to amplification of a perturbation that displaces the two vortices, through self and mutual induction. The preferred instability mode induces symmetric spanwise oscillations, in a varicose manner, rather than sinusoidal, of the trailing vortices before nonlinear evolution results in the vortices pairing into ring vortices (Crow, 1970; Breitsamter, 2011). For Gaussian vortices, the most amplified wavelength of this instability is approximately 8 times the spanwise separation distance between the vortices. The two streamwise vortices in an aircraft’s wake originate with a larger separation to core size compared with those of a HST, which may result in differences in how, or whether the instability manifests. In addition, the length of a HST, which allows the surface boundary layer to grow considerably together with the lack of focus on aerodynamic lift, provides a very different set of upstream conditions for the vortex pair development compared with those of an aircraft. Nevertheless, it is interesting to speculate whether the crow instability plays an active role in the downstream, but near-wake evolution of the vortex pair.

The work presented is an extension of a series of scaled wind-tunnel experiments, with results from high-frequency 4-hole dynamic-pressure cobra-probe mapping, surface-pressure measurements and flow visualisation published in Bell et al. (2016). These results showed that the pair of counter-rotating streamwise vortices seen in time-averaged fields exhibited signs of periodic unsteadiness.

This work provides insight into the dynamics of the pair of counter-rotating streamwise vortices trailing an Inter-City-Express 3 (ICE3) HST – a HST operating throughout Europe and China – through a variety of dynamic-pressure measurement techniques and analysis. This has provided a description of the unsteady dynamics of the large-scale near-wake of a HST and postulated causal mechanisms. This research, part of a collaboration between Monash University and Bombardier Transportation, aids in the identification, description and quantification of the flow mechanisms responsible for the slipstream characteristics which affect the safety and operation of modern HSTs. Ultimately, the insights provided by this work will aid in the design of future generations of HSTs.

2. Methodology

2.1. Experimental model

The high-speed train investigated in the presented work is a Deutsche Bahn Inter-City-Express 3 (ICE3). The external shape, and thus external aerodynamics, are the same as the Siemens Velaro HST. This HST is in operation throughout Germany, Netherlands, Belgium, Austria, Switzerland, Denmark, France, Spain, Turkey, Russia, and China. The HST Computer-Aided Design (CAD) model geometry is freely available from the TC 256 Secretariat held by the DIN Standards Railway Committee (FSF) (DIN Standards, 2014). The wide use of the ICE3 HST throughout the world and its modern aerodynamic shape that is similar to other current HSTs in operation, as well as the ready availability of the ICE3 geometry, makes it an ideal geometry for studying the flow structures proposed to be typical for HSTs.

A 1/10th-scale model of the ICE3 is utilised in the wind-tunnel experiment. The model’s dimensions are $5 \times 0.3 \times 0.4$ m ($L \times W \times H$), with a cross sectional area of ≈ 0.12 m². The model had four sets of bogies, no pantographs, no inter-carriage gaps and no heating, ventilation and air conditioning (HVAC) as the essential geometry – the gross external shape – is the focus of this investigation.

2.2. Experimental setup

The experimental setup aims to isolate the wake and resulting slipstream characteristics generated by the train’s essential generic geometry in an ideal environment. Thus, a HST is modelled travelling on a straight track over flat ground with no crosswind. The experiment was performed in the Monash University 1.4 MW wind tunnel (Fig. 1). The wind tunnel is a closed circuit design, with fixed pitch axial fans driven by a 1.4 MW quad-motor system capable of wind speeds between 5 and 65 m/s. The experimental setup in the wind-tunnel is presented in Fig. 1, and with greater detail in Fig. 2.

The coordinate system adopted is presented in Fig. 2. Streamwise position, x , is normalized by the model height (H), with $x = 0$ corresponding to the position of the tail. Cross-stream position, y , is normalized by the model width (W), with $y = -1/2$ corresponding to the left vertical edge and $y = 1/2$ to the right edge. Vertical position, z , is normalized by model height, with $z = 0$ corresponding to the top of the rails (TOR).

The 3/4 open test section measures $12 \times 4 \times 2.5$ (4.9H) m ($L \times W \times H$) and was fitted with a 0.6 m (1.5H) high splitter plane to reduce ground boundary layer effects, resulting in a cross sectional area above the splitter plane of 8.0 m².

A 1/10th scale Single Track Ballast and Rail (STBR) ground configuration (Fig. 2b) was included in the setup, with a height

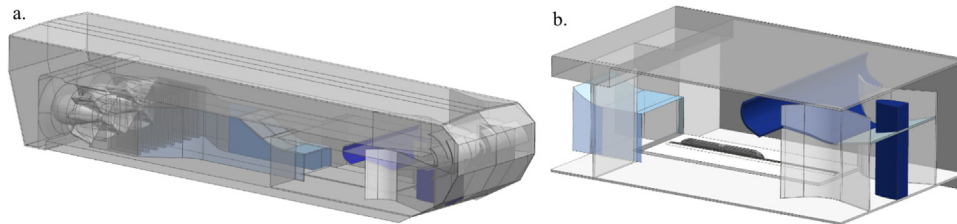


Fig. 1. (a) The Monash University 1.4 MW closed-return Wind Tunnel. (b) 1/10th-scale ICE3 model in the 3/4 open-jet test section. A 600 mm high splitter plate was utilised to reduce the ground boundary layer. Figure first appeared in Bell et al. (2016).

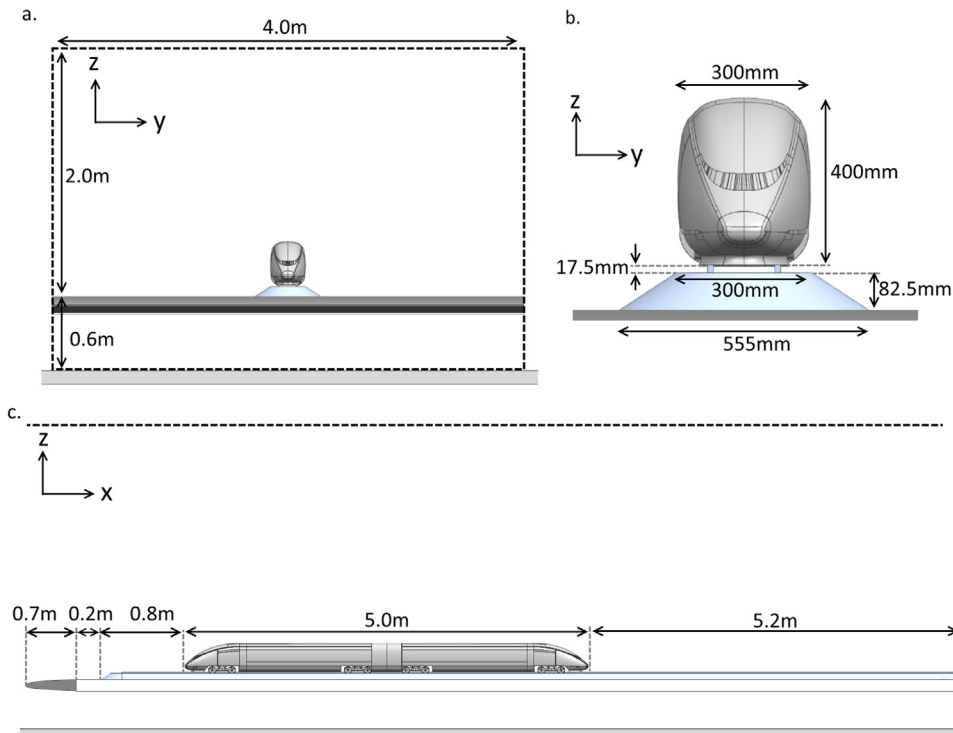


Fig. 2. The 1/10th-scale ICE3 model in the 3/4 open-jet test section of the Monash University 1.4 MW Wind Tunnel. A 600 mm high splitter plate was utilised to reduce the ground boundary layer. Figure first appeared in Bell et al. (2016).

of 100 mm ($0.2H$), and upper and lower widths of 300 mm ($1W$) and 555 mm ($1.85W$) respectively, adhering to the EN (CEN European Standard, 2009). The leading edge of the STBR had a front angle equivalent to the side angle (37°) swept 180° . Velocity measurements established no separation occurred over the leading edge of the STBR.

The model was supported above the STBR by 6 pairs of $0.05H$ (20 mm) diameter cylindrical supports, in line with the wheels in the bogies, at $x = -12, -8.5, -6.5, -4.5, -3.5$ and $-1.5H$.

The test-section was characterised in the yz plane over the range of $y = \pm 3.3(W/2)$, $z = -0.25 - 2.25H$ at $x = -12.5, -6.25H$, and $0H$ (the locations of the nose, mid-length and tail of the train), through 4-hole dynamic pressure measurements, as described in Section 2.3. These established that the test section was within the potential core of the jet from the wind-tunnel nozzle and not exposed to the shear layers of the 3/4 open-jet, and that the flow was uniform, having less than $\pm 1\%$ deviation of velocity, and did not contain the dominant frequencies found within the wake of the vehicle.

The maximum blockage ratio was $\approx 2\%$ above the splitter plate, including blockage due to the traverse and STBR. Thus, blockage effects are expected to be negligible, and no blockage corrections were applied. The approximate turbulence intensity (I_{tuvw}) above the wind tunnel boundary layer was 1.6%.

The length-to-height ratio of the scaled model was $L/H = 12.5$, which is smaller than a typical operational full-scale HST with a $L/H = 25 - 50$. This is necessary to allow as large a scale model – in terms of width and height – as possible in the test section, in order to achieve relevant high Reynolds numbers. Reduced L/H is also a limitation of moving model experiments for similar practical reasons. The high L/H of HSTs also presents a challenge numerically, as although technically they are not limited by physical space considerations, the associated computational requirements with increased L/H typically comes at the cost of Reynolds number and resolution. The effects of employing reduced L/H have been acknowledged in the literature (Weise et al., 2006), yet only recently has L/H been partially investigated by Muld et al. (2013). However, the full effect of

reduced L/H has yet to be explicitly quantified.

The sensitivity of the results to Reynolds number over the range $Re_w = 0.5 \times 10^6 - 1 \times 10^6$ is discussed in the results section. Reynolds number is calculated using width as the characteristic length, and freestream velocities over the range of 25–48 m/s. However, noting that the Reynolds numbers achieved in the experiments are still significantly smaller than full-scale Reynolds number of 17×10^6 which corresponds to a full-scale train travelling at 300 km/h.

The stationary surface of the splitter plate on which the STBR and train rest is acknowledged by the authors as an experimental limitation. This results in a boundary layer that develops along the ground that is not present in full-scale HST operation. The measured displacement thickness of the boundary layer was $\delta^*/H = 0.006$ and 0.035 at the models nose and tail positions respectively in an empty tunnel above the splitter plate. It is proposed that the flow structures of interest, the pair of streamwise vortices in the near-wake of the HST, are only affected by the ground boundary layer to a small degree. This is indicated by investigations of passenger automotive vehicles with wake structures analogous to HSTs, experimentally (Strachan et al., 2007) and numerically (Krajnović and Davidson, 2005), however, the insensitivity of a HST's wake has not specifically been established to date. As the model is also situated above a scaled ballast and rail, the distance between the model and the developing ground boundary layer is increased, further reducing any deleterious effects. As such, the general principles and findings presented are representative of that which occurs at full-scale for a HST in operation. The authors have previously discussed the influence of the stationary floor on streamwise vortices in a HST wake in Bell et al. (2014).

The boundary layer over a HST has been established as highly three dimensional (Baker, 2010), with the side boundary layer being sensitive to distance above the ground. Thus the side and roof boundary layers were measured and analysed as 2D boundary layers for simplicity, as previous researchers have done (Baker, 2010; Muld et al., 2013). The displacement thickness of the boundary layer at $x = -2.5H$ at the side ($z = 0.5H$) and roof ($y = 0(W/2)$) was $\delta^*/H = 3.12 \times 10^{-2}$ and 2.82×10^{-3} respectively. These correspond to momentum thicknesses of $\theta/H = 2.50 \times 10^{-2}$ and 2.70×10^{-3} for the sides and roof respectively. The sensitivity of results to the boundary layer thickness, expected to be dependent on L/H and to a lesser extent Reynolds number, is not investigated in the work presented.

2.3. Dynamic pressure measurements

Quantitative time-average and unsteady flow characterisation was performed through a variety of dynamic-pressure measurements. Each of the measurement setups consisted of pressure probes connected by tubing to differential pressure transducers in a 128 channel Dynamic Pressure Measurement System (DPMS).

In these systems, the phase and amplitude of the pressure measured by the transducer is distorted from the true pressure at the desired measurement point. This distortion occurs due to resonant characteristics of the tube (Iberall, 1950). In this experiment, the amplitude and phase response for each measurement was corrected using the *inverse transfer function* (ITF) method (Irwin et al., 1979). The frequency response of the pressure measurement system was determined theoretically using the method outlined by Bergh and Tijdeman (1965) for the total-pressure and 4-hole array, and experimentally for the 4-hole cobra-probe. This method of correction is common in similar dynamic-pressure measurements in applied aerodynamics research such as Vino et al. (2005) and Gilhome et al. (2001). Irwin et al. (1979) have shown through experiments that the ITF method reduces the average magnitude of error – defined as the average percentage difference of pressure at each discrete time-step – between the true and the measured pressure from 9.6% and 27.4% to 1.6% and 4.1% for tubing systems of 0.6 m and 3 m respectively – covering the range of tube lengths utilized in this experiment.

Two characteristic frequencies of the uncorrected frequency response are the frequency of the primary peak in the amplitude response, and the frequency where the amplitude response falls below 0.4. The frequencies where the primary peak in amplitude occurred were $St_w = 0.43$, 0.36 and 3.9 (50, 42 and 450 Hz) for the 4-hole probe array, total-pressure array and the 4-hole cobra probe described below respectively. The frequencies where the amplitude response fell below 0.4 were $St_w = 6.7$, 6.9 and 24 (780, 810, and 2250 Hz) for the 4-hole probe array and total-pressure array respectively. The dominant frequencies were expected to be in the range of $St_w = 0.1 - 0.25$ from the existing literature (Pii et al., 2014; Muld et al., 2012; Schulte-Werning et al., 2003). This corresponded to frequencies in the range of 10 – 50 Hz in the scaled wind-tunnel experiment when scale and velocity were considered. Thus, the frequency response of the pressure measurement systems is suitable for the range of frequencies of interest.

The sampling frequency was limited to $f_s = 1000$ Hz to prevent overloading the data acquisition system due to high bandwidth from multiple simultaneous measurements. This sampling rate in the 1/10th-scale experiments with freestream velocities of 25–45 m/s corresponds to 333 – 185 Hz for a full-scale, operational HST travelling at 300 km/h. Measurements had sampling times of 60 s.

2.4. Total pressure two-dimensional array

A two-dimensional array in the yz plane of 120 total pressure probes, simultaneously measured, connected to the DPMS, was developed and used to measure the unsteadiness of the wake. The probes had a spatial resolution of $0.05H$ ($0.125(W/2)$).

As the probes are forward facing and measuring in a region where the flow exhibits some degree of pitch and yaw, true total pressure of the flow is not measured, rather it is the summation of the dynamic pressure associated to the streamwise direction, u component of velocity, and static pressure. This pressure, P_i , was converted to the coefficient of pressure using

total, P_t , and static pressure, P_s from an upstream reference pitot-static tube:

$$C_p = \frac{P_i - P_s}{P_t - P_s}. \quad (1)$$

Calibration of the total pressure array (TPA) in an unobstructed test section being yawed up to $\pm 45^\circ$ found up to $\pm 15^\circ$ angle the cosine relationship of total pressure derived from the u component was consistent. Thus where the flow exhibits pitch or yaw of above $\pm 45^\circ$ degrees, the measurements are only a proportion of the dynamic pressure associated to the streamwise direction and static pressure.

The TPA is an additional source of blockage in the wake of the model, at 1.2% of the jet cross-sectional area. Surface pressure measurements on one half of the tail, published in Bell et al. (2016), were performed with the x position of TPA varied from $x = 1$ to $6H$ from the tail was performed. Results showed the overall pressure distribution shape did not change, however an average increase in pressure across the 120 taps with decreasing x position of TPA. At $x = 1H$, the average increase in the coefficient of pressure was 0.04, which is less than 10% of the range of pressures over the tails surface.

2.5. 4-Hole probe one-dimensional array

The one-dimensional array consisted of 17 4-hole dynamic pressure probes connected to the DPMS. The probe heads were $0.015H$ (6 mm) in diameter with 1.0 mm diameter holes. The probes were positioned in the spanwise direction with spacing of $0.3(W/2)$ (50 mm). Sensitivity of the probes to spacing, through repeated experiments with spacing 50 – 200 mm, concluded this spacing experienced negligible interaction between the probes. The probes were supported by a circular cylinder of diameter $0.04H$ (16 mm). The probe heads protruded $0.29H$ (115 mm) upstream of the cylindrical support (7.2 support diameters).

The probes were calibrated in separate experiments performed in a clean test-section in the same manner as Chen et al. (2000), Hooper and Musgrove (1997), and Vino et al. (2005). This involved pitching and yawing the probes in increments of 1 and 2° in the $\pm 20^\circ$ and $>20^\circ$ ranges respectively in a known flow to create calibration surfaces for yaw, pitch, total and static pressure based on the pressure ratios between the 4 holes. These calibration surfaces are then referenced to infer the yaw, pitch, total and static pressure the probes measured in the current experiment.

The velocities measured by the 4-hole probes, and cobra probes outlined below, have a train-fixed frame-of-reference (TF) in the wind tunnel. The component of the velocity in the x direction (u) was converted to the ground-fixed frame-of-reference (GF), the perspective of a stationary observer that experiences slipstream, and normalized against the freestream velocity:

$$u_{GF} = 1 - \frac{u_{TF}}{u_\infty} \quad (2)$$

The reference velocity, u_∞ , was calculated from an upstream reference pitot-static tube, corrected to the model's position through a dynamic pressure factor.

2.6. 4-Hole cobra probe measurements

Measurements were taken with a 4-hole dynamic-pressure probe (cobra probe). The cobra probe is capable of determining velocities with the accuracy of ± 1 m/s within a $\pm 45^\circ$ cone angle. However, it is not capable of identifying reversed flow (Hooper and Musgrove, 1997). An indication of the percentage of flow that is outside its calibrated cone of acceptance is provided by the probes accompanying software, in all cases reported $>95\%$ of measurements were within the cone of acceptance.

In the experimental results presented, a cobra probe was mounted in the wake at $x = 0.5H$, $y = 0.55(W/2)$, $z = 0.25H$ and used as a control signal for phase-averaging. Samples of 60 s at 1000 Hz were obtained simultaneously with other dynamic pressure measurements outlined below.

3. Results

3.1. Wake topology of a HST

A pair of counter-rotating streamwise wake vortices, a feature well-established in literature, is shown from cobra-probe measurements in the time-average wake of the ICE3 HST (Fig 3a). These vortices are identified by (v, w) vectors, streamwise vorticity, ω_x , and the vortex identifiers Γ_1 and Γ_2 . The scalar Γ fields quantify the change in the angle of velocity vectors moving in a circuit around each point. These fields attempt to distinguish between rotation- and shear-dominated vortical flow. For Γ_2 , the local convection velocity is removed prior to calculation of the angles, making this measure Galilean-independent. A vortex boundary is defined as $r_2 = 2/\pi$ (Graftieaux et al., 2001), and a vortex core is defined as the maximum of Γ_1 . These parameters are commonly used to define a coherent vortex (Graftieaux et al., 2001; Jeong and Hussain, 1995).

Measurements at additional yz planes were analysed in detail in Bell et al. (2016), which indicated the vortices moves

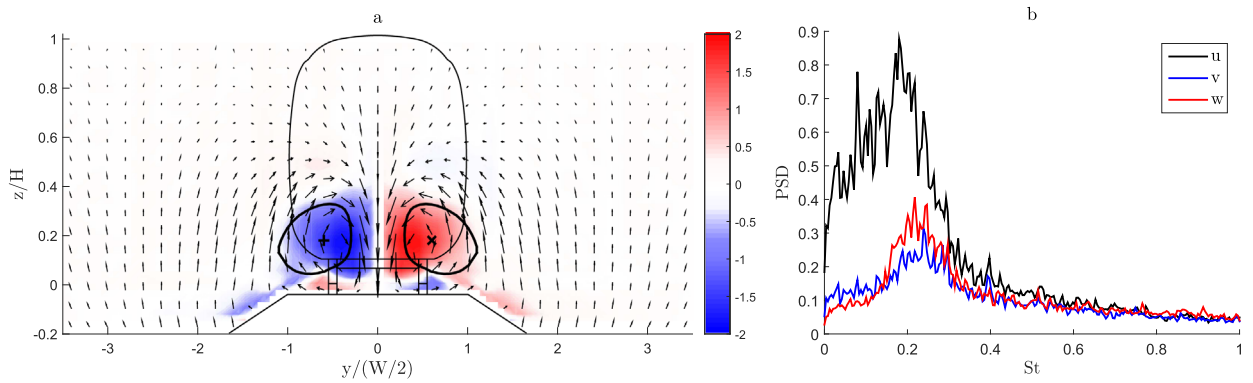


Fig. 3. (a) Time-averaged v , w , vectors, streamwise vorticity, ω_x , colourmap and $\Gamma_2 = 2/\pi$ contour line measured in the yz plane at $x = 1H$. (b) Power spectral density of u , v , w velocity components in the wake at $x = 0.5H$, $y = 0.55(W/2)$, $z = 0.25H$. Subsets of figure first appeared in Bell et al. (2016).

downwards and outwards from the centreline, consistent with mutual induction and induction with image vortices below the ground plane. Additionally, analysis of all cobra probe measurements traversed in the yz plane identified regions of high turbulence and power spectral density at the dominant frequency of $St_w = 0.2$, although occurring at different positions in the wake for the different velocity components: in the streamwise vortex cores for u , in a spanwise band for v and a central region around the tail tip for w . Coupled spanwise vortex shedding off the sides of the vehicle, and vertical vortex shedding off the tail tip could explain the v and w results respectively. The periodicity of these two features could in turn affect the streamwise vortices and hence explain the periodicity of u velocity within the vortex cores.

Periodicity is also evident in the frequency analysis of the control cobra probe positioned at $x = 0.5H$, $y = 0.55(W/2)$, $z = 0.25H$ situated in the core of one of the streamwise vortices (Fig. 3b). A Fast Fourier Transform (FFT) was utilized to convert the time signal to the frequency domain. A Hamming window methodology was applied using 16 windows and 50% overlap. The average of the multiple windows was then taken in an attempt to reduce spectral leakage.

In Fig. 4a, the time-averaged total pressure measured by the TPA is presented with a region of low total pressure that starts directly behind the vehicle and moves outwards with downstream distance. The standard deviation of total pressure (Fig. 4b), clearly associates two regions of high standard deviation to the streamwise vortices identified from cobra-probe measurements.

Although the boundary layer does not appear to strongly influence these results, the presence of the stationary floor does present different flow conditions and the wake structure is expected to show some differences to a moving-floor setup characteristic of a real train. It is expected that the stationary floor results in an increased flattening of the overall wake structure. This is a common finding for longitudinal vortices embedded in or moving towards a boundary layer (Westphal and Mehta, 1989; Pauley and Eaton, 1988; Lödberg et al., 2009). The distortion of the ground boundary layer by a vortex leads to rapid diffusion of streamwise vorticity resulting in the growth of the vortex core (Pauley and Eaton, 1988), which increases the flattening of the core (Westphal and Mehta, 1989; Lödberg et al., 2009).

Spectral analysis of total pressure measured by the TPA (Fig. 5a) at two points either side of the xz symmetry plane located in the regions of high standard deviation in Fig. 4, at $x = 1H$, $y = \pm 1(W/2)$, $z = 0.2H$, display the same dominant frequency identified in the cobra-probe measurements of $St_w = 0.2$. The PSD of a total pressure probe measuring in the freestream, at $x = 1H$, $y = 0(W/2)$, $z = 0.75H$, shows no peak at this dominant frequency.

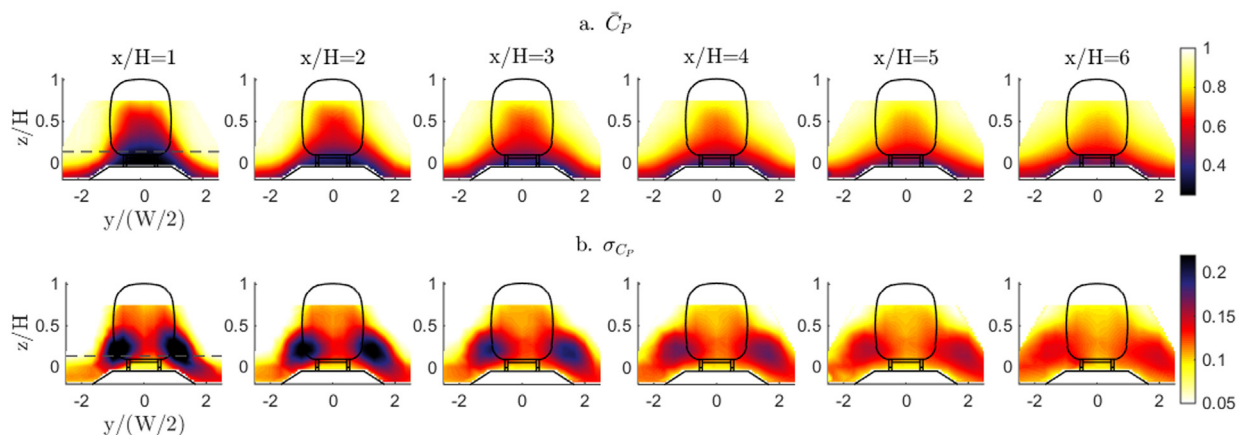


Fig. 4. (a) \bar{C}_P and (b) σ_{C_P} obtained from the total pressure array for cross-stream (yz) planes at downstream positions $x = 1, 2, \dots, 6H$.

Cross-correlation of the signals at the two symmetric points identifies (Fig. 5b) that they are effectively 180° out-of-phase. The non-dimensional time period corresponding to $St_w = 0.2$ is $tV/L = 5$. At zero lag, the correlation is at its maximum magnitude negative value, and at half the period, ($tV/L = 2.5$), the correlation is at its maximum positive value.

The dominant wake frequency of $St_w = 0.2$ and the wake topology were independent of Reynolds number over the range $Re_w = 0.5 \times 10^6 - 1 \times 10^6$ tested.

3.2. Spanwise dynamics

A bulk spanwise sinuous oscillation of the wake is observable in the time variation of the total pressure coefficient along a spanwise (y) line through the streamwise vortices as shown in Fig. 6. This is obtained from the yz plane measurements at $x = 1H$, from 17 total-pressure probes located at $z = 0.2H$. This spanwise line cuts through the two regions of high standard deviation visible in Fig. 4b associated with the streamwise vortex pair. The oscillation is clearest at $z = 0.2H$, however, was

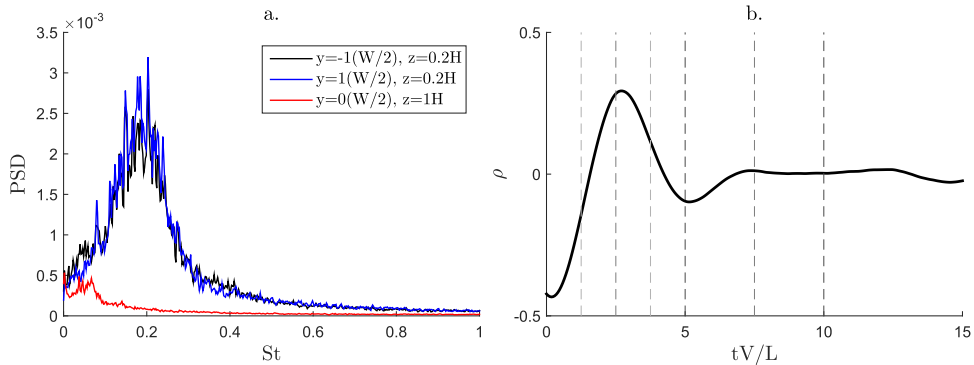


Fig. 5. Total pressure array results at $x = 1H$. (a) Power spectral density of total pressure measured by 3 selected probes and (b) cross-correlation of total pressure signals of 2 symmetrically placed probes either side of the plane of symmetry.

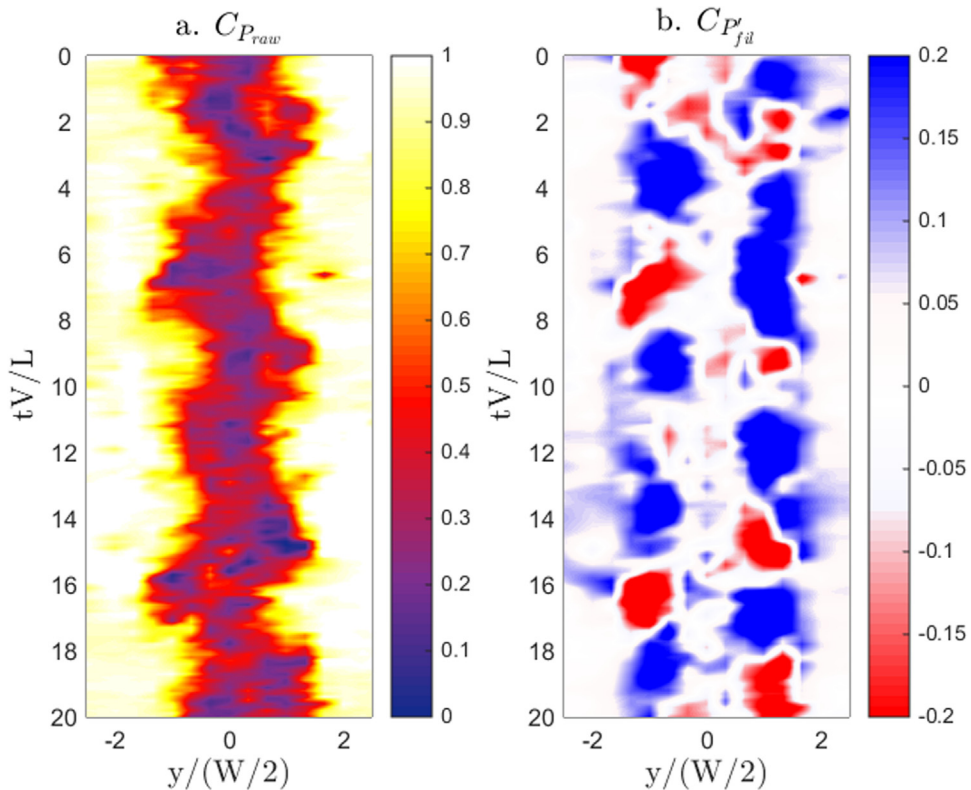


Fig. 6. (a) Raw, unfiltered C_p and (b) C_p after low-pass filtering with $St_w < 0.7$. Here, $x = 1H$, $z = 0.15H$, as indicated by the dotted grey lines in Fig. 4.

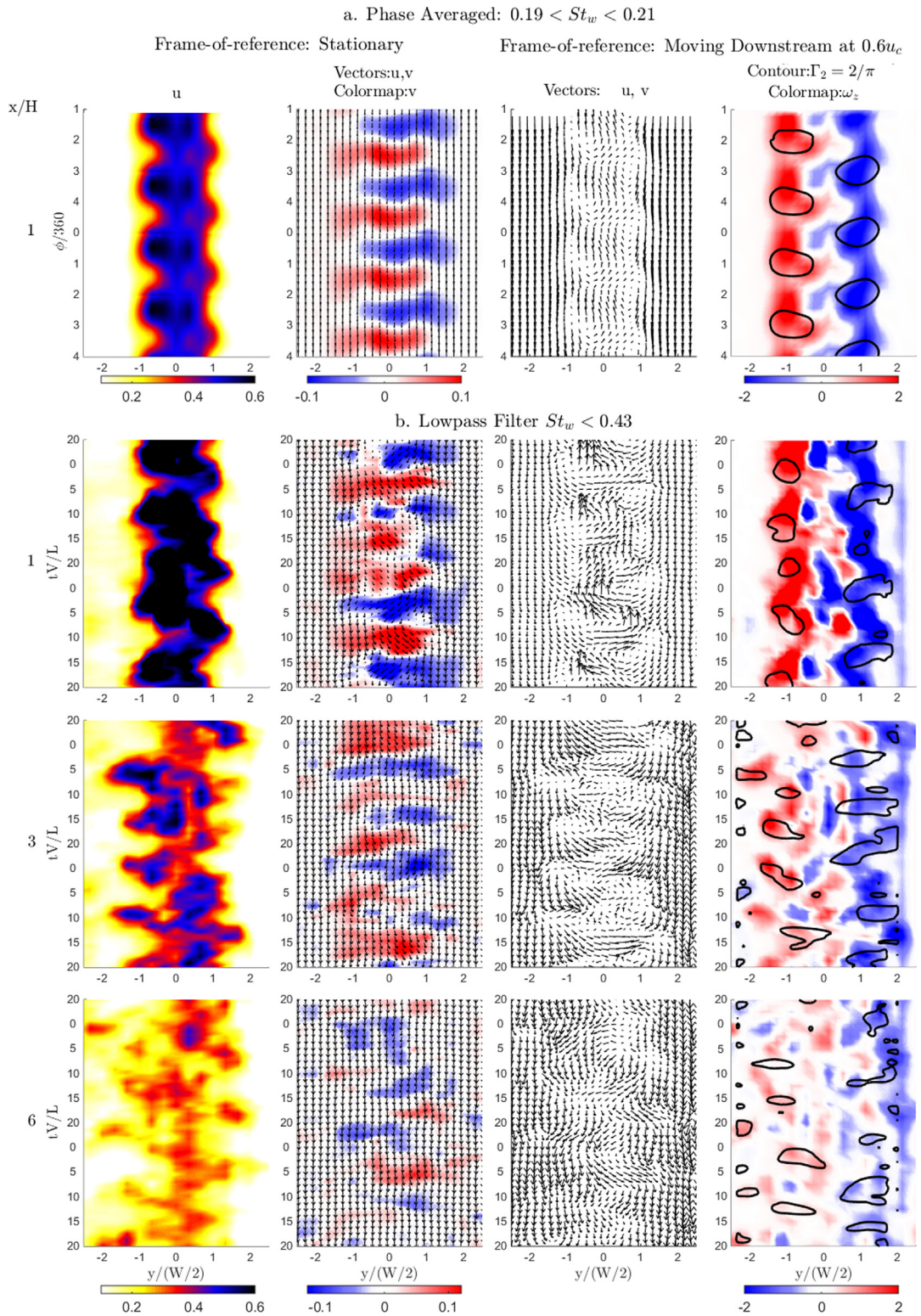


Fig. 7. Velocity, vorticity, and vortex identifier $\Gamma_2 = 2/\pi$ of data measured by the spanwise array of 17, 4-hole dynamic pressure probes at $z = 0.2 H$. (a) Phase-averaged results measured at $x = 1H$ from data with a single-pole $0.19 < St_w < 0.21$ bandpass butterworth-filter - based on the dominant frequency of $St_w = 0.2$. (b) Transient data with a single-pole butterworth lowpass-filter $St_w < 0.43$ at $x = 1, 3, 6H$.

also observed in spanwise lines at heights within the high standard deviation regions at all x positions measured.

The results are presented as raw C_p , as well as the fluctuating pressure, C_p , filtered with a single-pole, Butterworth lowpass filter, of $St_W < 0.7$. The oscillations are directly associated to alternating regions of positive and negative fluctuations in pressure that are 180° out-of-phase in the spanwise plane (Fig. 6b). A visible time period of $tV/L \approx 5$, which corresponds to a frequency of $St_W = 0.2$, is evident in these results.

Data from a spanwise array of 17 4-hole probes at a height of $z = 0.2H$, located at $x = 1, 3, 6H$, and filtered with a single-pole Butterworth lowpass filter $St_W < 0.43$ is presented in Fig. 7b. The same spanwise-oscillation as demonstrated in the TPA results is observed at all x positions, however at $x = 1H$, the causing mechanism is identified. The oscillation in the streamwise, u , velocity component is linked to the oscillating direction of spanwise velocity, v , over time, when viewed from the stationary frame-of-reference.

Further insight into the streamwise dynamics behind a HST are gained when visualising the flow while moving with a convection velocity. In this case, a convection velocity $u_c = 0.6 u_\infty$ was used, as this represented the average streamwise velocity in the area of high streamwise and spanwise fluctuating velocity ($y \approx \pm 1(W/2)$).

Velocity vectors of u and v in the moving frame-of-reference clearly identify vortices of alternating signs. Colourmaps of vorticity in the xy plane, ω_z , and $\Gamma_2 = 2/\pi$ contour lines also identify the alternate vortices. A visible time period of $tV/L \approx 5$, which corresponds to $St_W = 0.2$, is also evident in these results. Such structures were convected past the 1D array of 4-hole probes over time, and would exist in the xy plane with additional spatial variation. There are limited signs of the regular vortices in the spanwise plane further downstream at $x = 3$ and $6H$.

The data from the spanwise array of probes was phase-averaged using a single cobra probe, located at $x = 0.5H$, $y = 0.55(W/2)$, $z = 0.25H$, positioned in the region of high standard deviation, and used as a control signal to phase-average the array of 4-hole probe data. A single-pole $0.19 < St_W < 0.21$ bandpass Butterworth filter, based on the observed dominant frequency of $St_W = 0.2$, was applied to the control signal, as well as the corresponding 4-hole data.

A spanwise slice of the phase-averaged results from $x = 1H$, $z = 0.2H$ are presented in Fig. 7a and exhibits the same features as the filtered data in Fig. 7b at $x = 1H$, the alternating spanwise vortices convected in the wake.

3.3. Streamwise dynamics

A phase-averaged description of velocity in the yz plane using the 4-hole array data was subsequently constructed. This was done by taking each set of temporal data from the spanwise array of 17 probes, measured at 13 different heights, and using a control cobra probe kept at a constant position to allow phase averaging the signals between the different heights.

The wake structure in the yz plane at $x = 1H$ at phase angles of $\phi = 80, 170, 260$ and 350° is presented in Fig 8d, e, f, and g. These phase angles provide a representation of the full range of dynamic motion in the wake. The time-average wake structure is presented in Fig 8a–c for reference. The resultant slipstream velocity visibly oscillates left to right over the complete phase. The projected (v, w) velocity vectors for each phase angle identifies that the spanwise oscillation corresponds to the alternating dominance of the left and right streamwise vortex; this is clearly depicted by images for $\phi = 80^\circ$ and $\phi = 260^\circ$, which are the two opposing phase angles where the maximum difference between the two vortices occurs. The dynamics of the two streamwise vortices, alternating in moving upwards and outwards to downwards and inwards, are visible through the vorticity, ω_x , colourmaps and $\Gamma_2 = 2/\pi$ contour lines, and $\max[\Gamma_1]$ in Fig. 8c. The dynamic motions of the vortex cores are also illustrated in Fig 9a as iso-surfaces of $\Gamma_2 = 2/\pi$.

The changing size of each streamwise vortex is quantified in Fig. 9b, where the area within the $\Gamma_2 = 2/\pi$ boundary is presented over the $St_W = 0.2$ phase cycle. This result clarifies the periodic alternating-dominance of the two streamwise vortices, where the dominant vortex is larger in size and located at a higher, more central position relative to the other.

The spatial dominance is not in-phase with the magnitude of circulation within each vortex (Fig. 9c). Circulation was calculated using Stokes' theorem, from the vorticity over the area within $\Gamma_2 = 2/\pi$ at each phase angle. The results show that the circulation in each vortex increases/decreases out-of-phase relative to each other, however an increase in circulation occurs when both vortices have the same area and are located in relative symmetry.

The periodic-fluctuating components of cross-stream velocity, ($\Delta v, \Delta w$), which represent the difference between phase-average and time-average cross-stream velocity components:

$$\Delta v = v_{\phi=i^\circ} - \bar{v}, \quad (3)$$

$$\Delta w = w_{\phi=i^\circ} - \bar{w}, \quad (4)$$

are presented as velocity vectors in Fig. 8d.

These results associate a strong Δv region that contributes to the lower portion of the dominant streamwise vortex (Fig. 8b). This region of periodic-fluctuating spanwise velocity occurs at a higher position than the spanwise velocity that contributes to lower half of each time-average streamwise vortices (top of Fig. 8b). This periodic-fluctuating spanwise velocity contribution is therefore also what encourages the dominant streamwise vortex to move to a higher position, as the vortex moves to align the lower spanwise region with the fluctuation. This interaction is visible in the combination of colourmaps of the spanwise velocity, v , in the ϕy plane at $z = 0.2H$ with the yz plane at $\phi = 260^\circ$, with additional (v, w) projected velocity vectors presented in Fig. 10. This figure shows the spanwise fluctuation due to the spanwise vortex

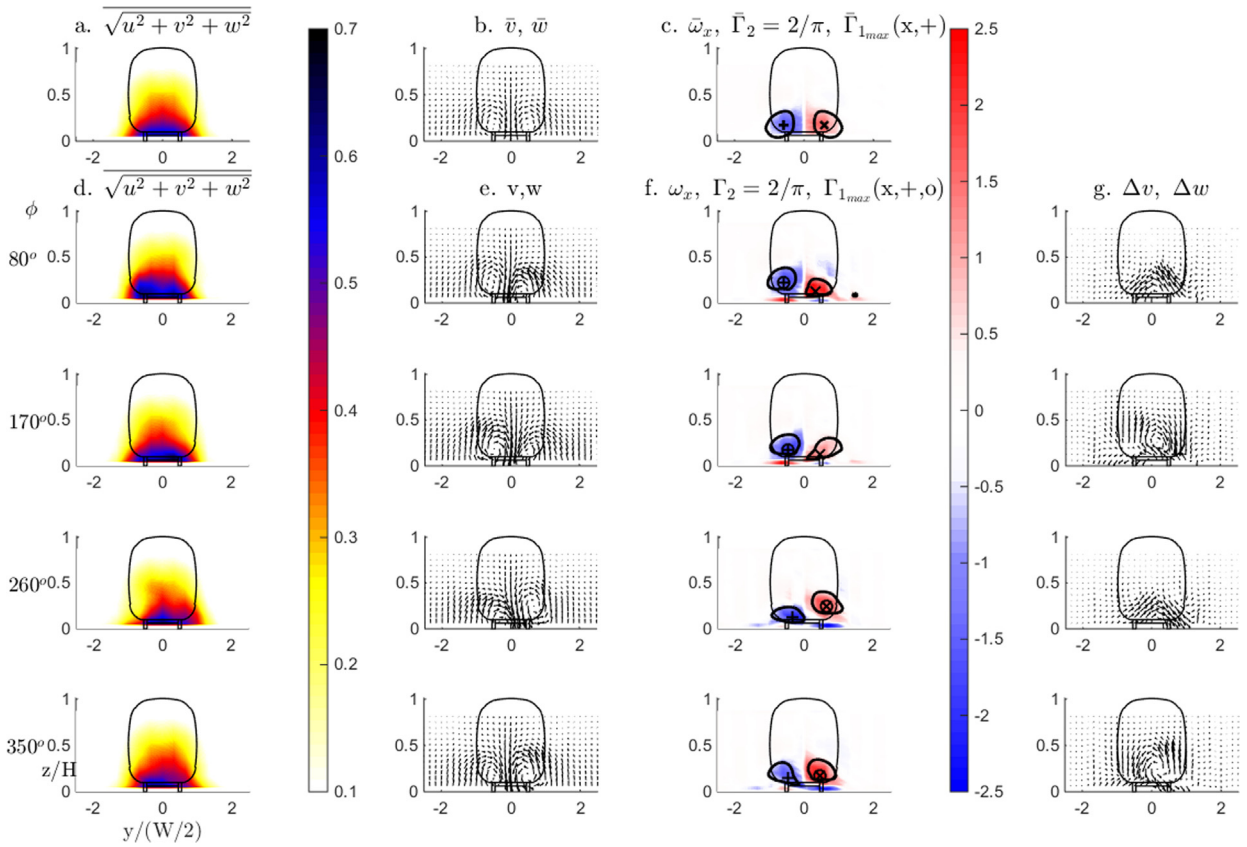


Fig. 8. Time-averaged (a–c) and phase-averaged (d–g) results from data measured by a spanwise array of 17, 4-hole dynamic pressure probes at $z = 0 - 1H$ in 13 steps at downstream position $x = 1H$. Phase angles, $\phi = 80, 170, 260$ and 350° are presented. (a and d) resultant velocity, (b and e) v, w vectors, (c and f) vorticity, ω_x and vortex identifiers $\Gamma_2 = 2/\pi$ and $\max[\Gamma_i]$ LHS: + and RHS: \times (the larger of LHS and RHS is denoted by O), (g) $\Delta v, \Delta w$ velocity vectors. (a–c) are subsets of a figure that first appeared in Bell et al. (2016).

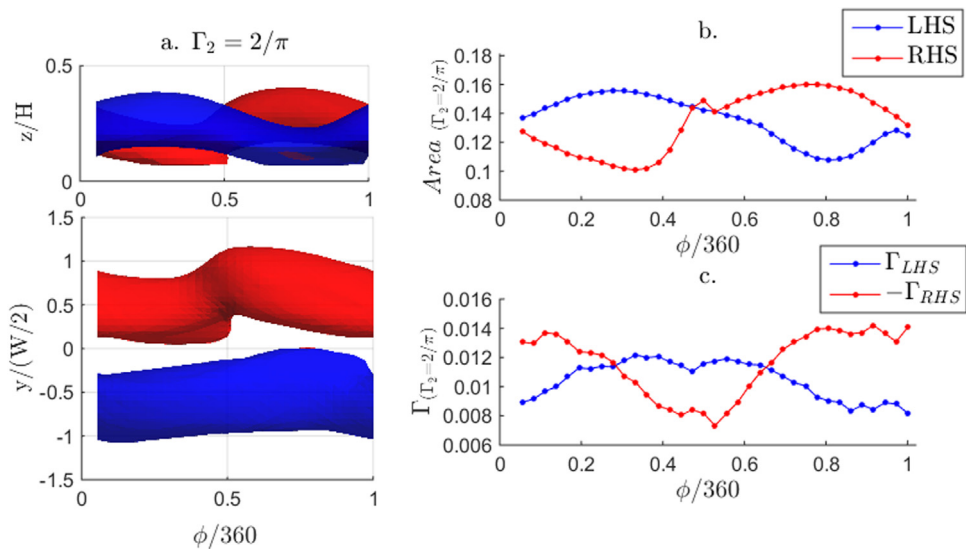


Fig. 9. (a) Iso-surface of $\Gamma_2 = 2/\pi$ over the $St_W = 0.2$ phase cycle. LHS (blue) and RHS (red) streamwise vortices. (b) Area of the LHS and RHS vortex core ($\Gamma_2 = 2/\pi$) and (c) circulation within the vortex core ($\Gamma_2 = 2/\pi$) over the $St_W = 0.2$ phase cycle. LHS (blue) and RHS (red) streamwise vortices. (For interpretation of the references to colour in this figure caption, the reader is referred to the web version of this paper.)

shedding observed in Fig. 7.

The periodic-fluctuating cross-stream velocity ($\Delta v, \Delta w$) identifies centred streamwise vortices of alternating sign at

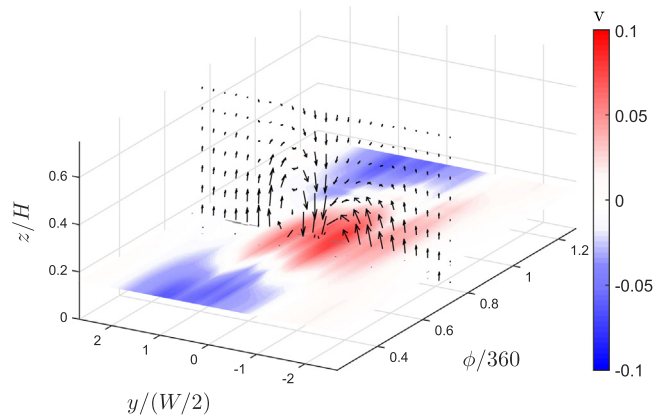


Fig. 10. Phase-averaged results of data measured by a spanwise array of dynamic pressure probes at $x = 1H$. Spanwise velocity, v , in the ϕy plane at $z = 0.2H$ presented with cross-stream velocity vectors at $\phi = 260^\circ$ showing the interaction between side vortex shedding and trailing streamwise vortices.

$\phi = 170^\circ$ and 350° when the transient streamwise vortices are positioned in relative symmetry. These can be associated with the increase/decrease in circulation of each of the streamwise trailing vortices, as this fluctuating vortex changes sign over the cycle.

From these results, the dynamics of the relationship between the apparent vortex shedding initiating at the sides of the train and the streamwise counter-rotating pair can be inferred. Initially, as a vorticity concentration is convected along the sides downstream into the wake, it is tilted so that the induced vertical velocity pushes the streamwise vortex upwards. Following this, as it is advected further downstream and is further tilted to align with the downstream direction, it merges with the streamwise vortex ceasing to exist as a coherent identifiable flow structure. This explains why the vortex shedding from the sides is only readily visible at $x = 1H$ (Fig. 7), and not further downstream, e.g., at $x = 3$ and $6H$.

The data collected by the pressure-probe array was also phase averaged for cross-stream planes at $x = 3$ and $6H$. Combined with phase-averaged fields at $x = 1H$ presented previously, this is presented as contour lines of $\Gamma_2 = 2/\pi$ and \overline{uvw} represented as different phase angles by blue to red lines in Fig. 11. In these results, the alternating dominance of the two streamwise vortices over a cycle and the effect on bulk slipstream remain visible and coherent at the positions further downstream in the wake.

The phase-averaging of the 4-hole data has not resulted in perfectly anti-symmetric results. This is expected to be due to the control cobra probe being positioned at $x = 0.5H$, $y = -0.55(W/2)$, $z = 0.25H$, to capture the fluctuating region of the wake. Thus, more coherent phase-averaged results would be expected in the $-y$ domain.

3.4. Mode decomposition of streamwise dynamics

Proper orthogonal decomposition (POD) (Lumley et al., 1967) following Sirovich's snapshot method (Sirovich, 1987) was performed on the fluctuating pressure array data to provide insight into the coherent dynamic features of the wake. POD has been used extensively in fluid dynamic research to identify dominant flow components by, e.g., Graftieaux et al. (2001), Perrin et al. (2007), and Muld et al. (2012), and more recently for HST wakes by Muld et al. (2012). The results are presented in Figs. 12 and 13.

Each individual mode contributes to the fluctuating pressure in the wake. The first 100 modes at each x position are ordered by the magnitude of their contribution to the overall fluctuating pressure in Fig. 12. These results, together with visualisations of the modes to check their coherence, indicate that up to 6 modes provide considerable coherent contributions to the fluctuating pressure at the six downstream positions at which data was recorded. The first mode is clearly dominant, with a significant contribution of fluctuating pressure of up to 24%. Its magnitude decreases further into the wake to 15% at $x = 6H$, as could be expected due to reducing coherence. The second mode also shows a progressive reduction in contribution to fluctuating pressure from 7% to 5% further in the wake. For higher modes however, this trend is reversed, with these modes having higher contribution further in the wake than closer to the rear of the train.

Spatial representations of the first 6 modes, ranked by magnitude of their contribution to the overall pressure fluctuation, are presented in Fig. 13 for each plane measured. Inspection of these results establishes that there are a number of types of spatial modes that exist in different orders at different positions in the wake. These have been labelled A–F and are described in Fig. 14 and annotated onto Fig. 13. These modes denote regions in space where fluctuations in total pressure occurs. These fluctuations can be inferred as movements in the size and position of the streamwise vortex pair (as illustrated in Fig. 14) through the association between high regions of standard deviation in the TPA results of Fig. 4 and the identified streamwise vortex pair from cobra probe measurements in Fig. 3a.

Mode A represents an alternating out-of-phase increase/decrease in size of the vortices belonging to the streamwise vortex pair. This mode is the most coherent and contains the largest contribution to pressure fluctuation at all measured x positions. Mode B represents the simultaneous increase/decrease in total pressure of the same structures, inferred as the

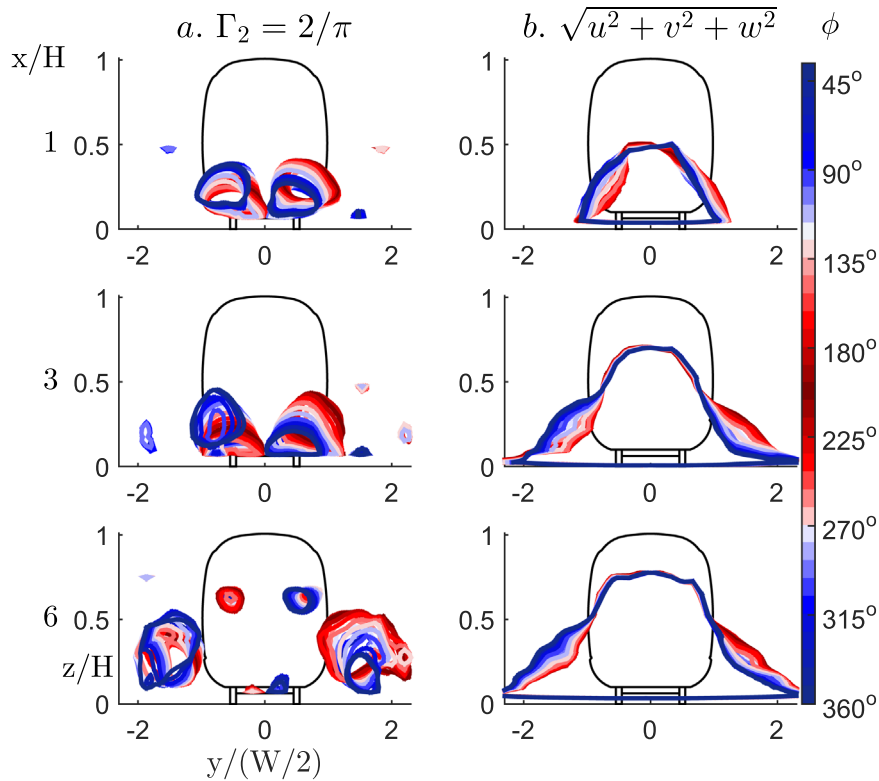


Fig. 11. Phase-averaged data measured by the dynamic pressure array at $x = 1, 3, 6H$. (a) Contour lines of $\Gamma_2 = 2/\pi$, (b) contour lines of $\sqrt{u^2 + v^2 + w^2} = 0.3, 0.1, 0.1$, at $x = 1, 3, 6H$. The entire $St_W = 0.2$ cycle is represented by transition from blue to red of the colourmap. (For interpretation of the references to colour in this figure caption, the reader is referred to the web version of this paper.)

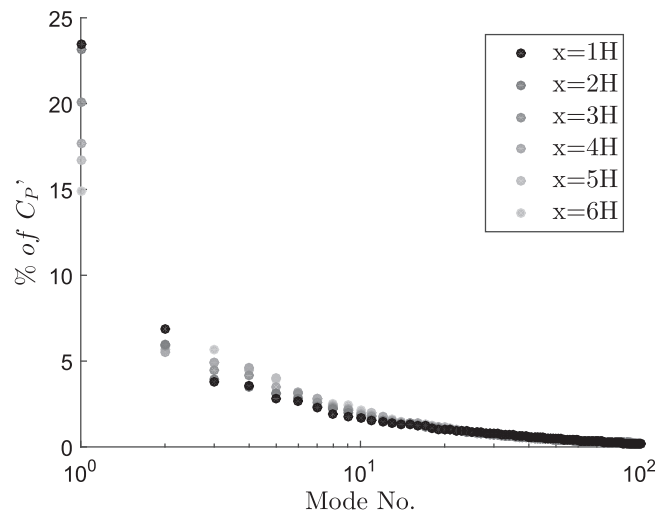


Fig. 12. TPA POD modes 1–100: % of contribution to the fluctuating total pressure in the yz plane at $x = 1$ – $6H$.

increase/decrease in size of the streamwise vortex pair. However, mode B is only coherent up to $x=4H$. Mode C represents the simultaneous/symmetric spanwise motion of the streamwise vortex pair. Modes D and E represent similar motions of the vortex pairs oscillation in the diagonal direction above the ballast shoulder, where D exhibits alternating, asymmetric oscillations and E exhibits simultaneous, symmetric oscillations. Mode F is similar to that of mode D, with alternating, asymmetric oscillations, however the motion is in the vertical direction. Modes C, D, E and F exhibit similar characteristics, each contains combinations of symmetric/anti-symmetric oscillations in the spanwise and vertical directions.

The most dominant modes, identified at $x = 1H$, become progressively less coherent on moving downstream in the wake. Mode A is visible at all positions, mode B up to $x = 4H$, modes C and D up to $x = 4H$ and modes E and F up to $x = 2H$. This can

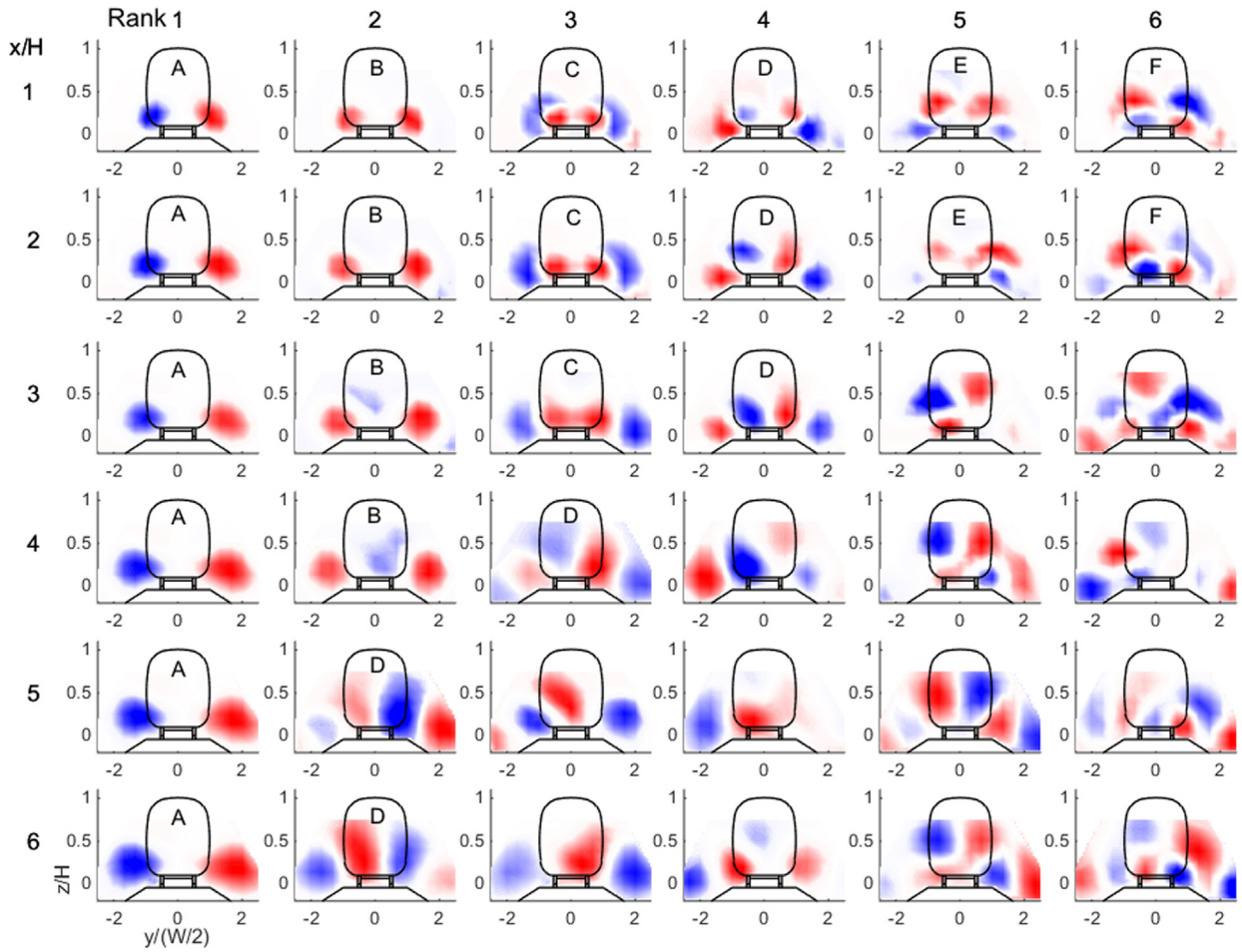


Fig. 13. POD modes 1–6 ranked by magnitude of contribution to pressure fluctuation from the TPA results in the yz planes at $x = 1:6$.

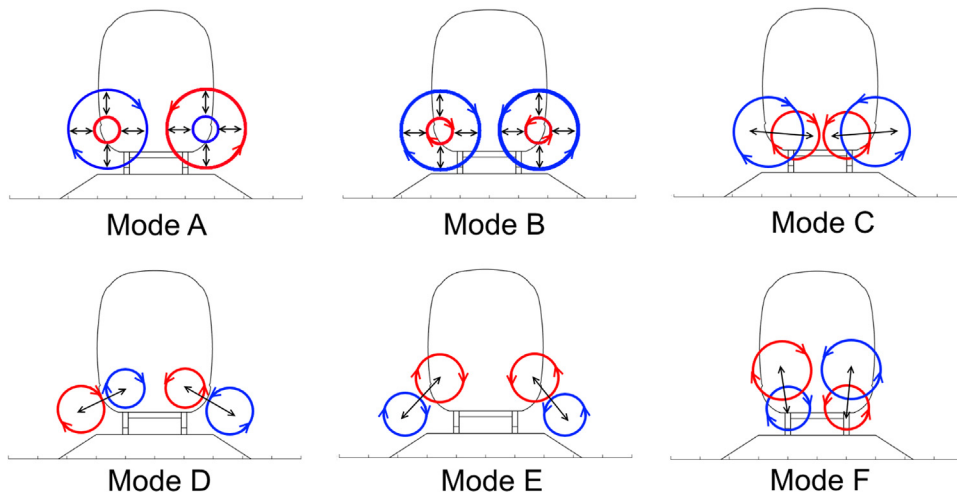


Fig. 14. Identifiable modes A, B, C, D, E, F associated to movement/oscillations of the streamwise vortex pair.

be attributed to mechanisms that cause these lower modes B–F being directly associated to flow structures developing at, or in close proximity to the tail, which lose coherence downstream. Modes A, D and F are asymmetric, while B, C and E are symmetric.

Mode D is unique in that it leapfrogs Modes B and C when ordered farther in the wake. At $x = 4H$, mode C is not

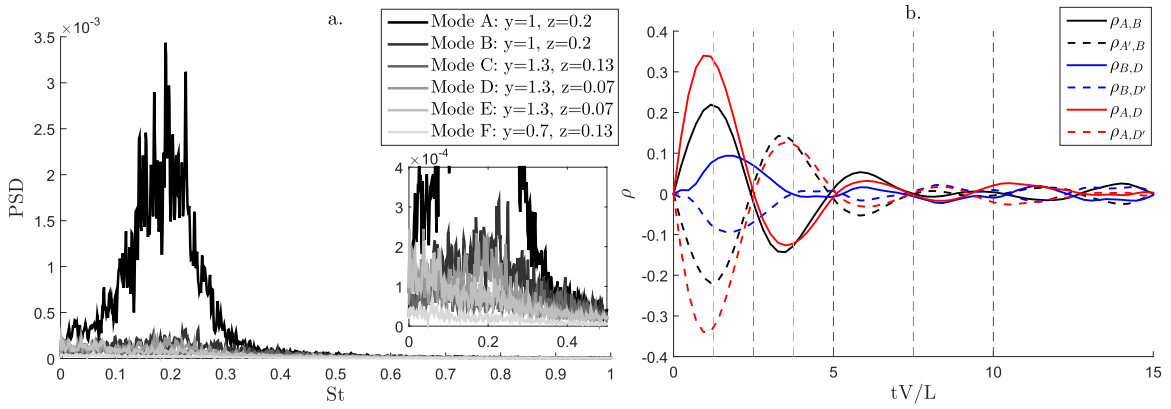


Fig. 15. (a) PSD of modes A–F at $x = 1H$. (b) Cross-correlation of signals in modes A and B, modes B and D, modes A and D.

apparent, and mode D is the third and last coherent mode when ordered. Similarly at $x = 5$ and $6H$ mode D is the second and last coherent mode as modes B and C do not occur at these x positions.

Spectral analysis of the POD modes A to F at $x = 1H$ is presented in Fig. 15a. Mode A exhibits the clearly dominant frequency of $St_W = 0.2$. Modes B and D also exhibit the dominant frequency of $St_W = 0.2$, however with a broader peak and at lower power. As modes A, B and D exhibit the same frequency as the data from measurements made without decomposition, this further strengthens the proposal that the modes can be linked with shedding from the sides of the train.

The spectral analysis was performed on 6 individual reconstructed total pressure signals, using each of the individual modes A–F, at the (y, z) positions associated with fluctuating regions for each mode in Fig. 13.

As modes A, B and D shared the same dominant frequency, cross-correlation of these signals was performed to determine their phase, relative to each other. The results are presented in Fig. 15b. Since modes A and D are antisymmetric modes, correlation of each side was calculated and denoted with a prime: A and A', D and D'. As mode B was symmetric, a signal from only one side was used in cross-correlation calculations. The non-dimensional frequency of $St_W = 0.2$ corresponds to a non-dimensional time period of $tV/L = 5$.

The cross-correlation results indicate that modes A and B are weakly correlated, 90° out-of-phase from each other. This infers that in between the spanwise oscillation left-to-right of mode A, mode B acts to increase/decrease the total pressure of both vortices simultaneously. Mode A is speculated to be associated with vortex shedding from the sides, thus having an antisymmetric effect on the wake. Mode B could be due to weaker shedding as the fluid advects downstream over the tail. This has a symmetric effect on the wake. Mode B occurs between maxima of mode A, when the wake is relatively symmetric, as might be expected. However, the relatively low correlation ($\rho = 0.2$) between these two features suggests this timing is not strong.

Modes B and D are out-of-phase $\approx 135^\circ$ with a very weak level of correlation ($\rho = 0.1$). Modes A and D have the highest level of correlation ($\rho = 0.35$) and are also 90° out of phase from each other. The dynamics inferred from this correspond to the diagonal oscillations over the ballast shoulder occurring between the alternating increase/decrease of the total pressure associated to the streamwise vortices.

3.5. 3D dynamics

The control cobra-probe was kept at the same position while the TPA was swept through the streamwise direction, enabling each of the 9 yz planes ($x = 0.5, 1, 1.5, 2, 2.5, 3, 4, 5, 6H$) measured to be phase-averaged relative to each other. From these TPA results, the motion of the streamwise vortices and spanwise dynamics identified by the 4-hole array measurements can be inferred.

The phase-averaged TPA data is presented in Fig. 16 by a filled contour in the xy plane over six phase-angles, which show the range of dynamic motion over the $St_W = 0.2$ cycle. A spanwise oscillation of the total pressure with clear sinusoidal motion is visible in the wake. These results, presented in 2D for clarity, are consistent with the spanwise TPA and 4-hole array results in 1D over time.

The TPA phase-averaged results are presented in 3D in Fig. 17 at 4 phase angles. The difference in pressure between the phase-average and time-average,

$$\Delta C_p = C_{p,\phi=i^\circ} - \bar{C}_p, \quad (5)$$

which identify paired 3D regions, presented as iso-surfaces of positive and negative deviations around the mean C_p that cause the spanwise-oscillation of the bulk total pressure. These pockets exist in alternating pairs and are convected down into the far wake where they start to lose coherence. This is the same dynamic movement as mode A of the POD analysis of TPA data in Fig. 14 and the spanwise fluctuating pressure in Fig. 6b. From the 4-hole array phase-averaged results, we can

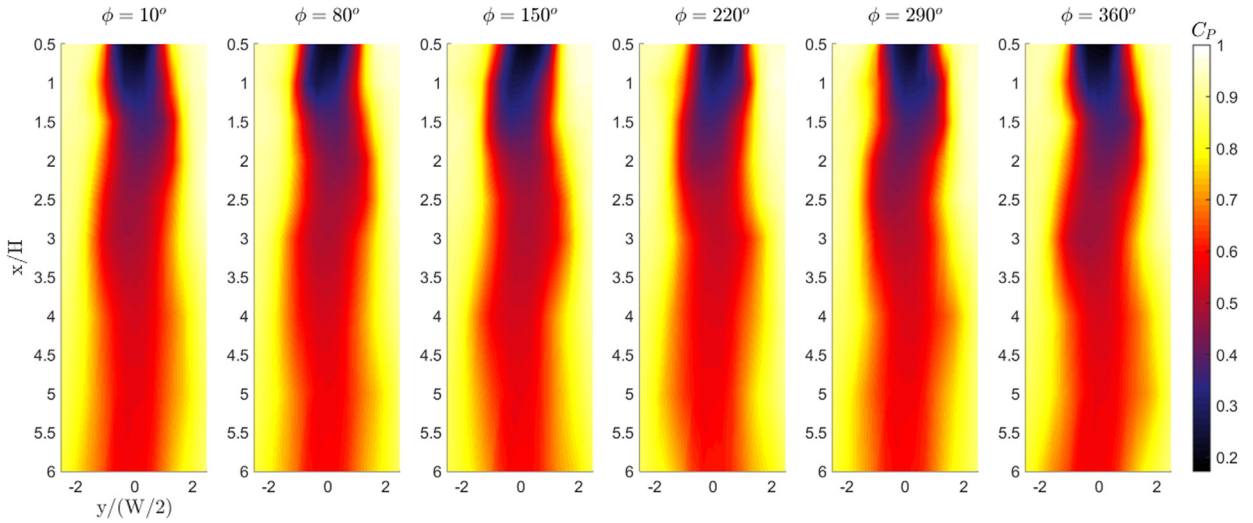


Fig. 16. C_p contours in the xy plane at $z = 0.15H$. Phase angles, $\phi = 10, 80, 150, 220, 290, 360^\circ$ presented.

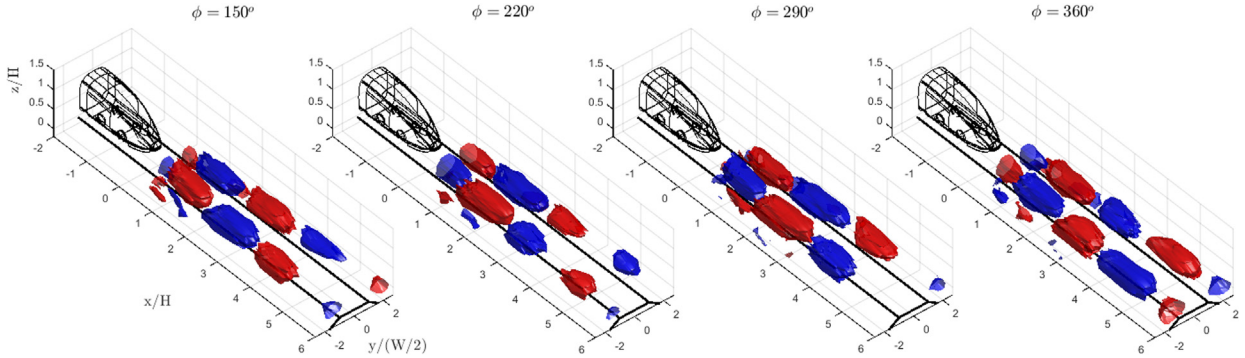


Fig. 17. Phase-averaged iso-surfaces of $\Delta C_p = \pm 0.02$ at phase angles of $\phi = 150, 220, 290, 360^\circ$.

infer that these alternating regions in total pressure are periodically alternating the size and position of the streamwise vortices.

The wavelength of this oscillation is $\lambda \approx 2.75H$. The spanwise separation distance of the counter-rotating streamwise vortex pair was determined from surface pressure and surface flow visualisations by Bell et al. (2016) to be $b \approx W/2$. Thus the wavelength is $\lambda \approx 7.3b$. The wavelength estimated from the dominant frequency of $St_W = 0.2$, using the freestream velocity, $u_\infty = 35 \text{ m/s}$ as the convection velocity, is slightly larger at $\lambda \approx 10b$. This difference can be attributed to the over-estimation caused using the u_∞ as the wake convection velocity. Interestingly, the wavelength and the type of oscillation are consistent with a Crow instability of the vortex pair, where the theoretical $\lambda_{Crow} \approx 8.6b$, and full-scale observations have identified $\lambda_{Crow} = 8 - 9b$ (Crow, 1970). In addition, finite-core size results in lowering of the preferred wavelength (Steijl and Hoijmakers, 2001) not inconsistent with the slightly lower value of $\lambda \approx 7.3b$ observed in this case. The interaction of the streamwise vortex pair and the image vortex pair in the ground is expected to contribute to their dynamics. The vertical spatial oscillation has similarities with vortex ‘rebound’ caused by induced upwards flow from the formation of secondary vortices at the ground (Barker and Crow, 1977; Leweke et al., 2016). Further, the development of the Crow instability has been observed to be sensitive to the height above the ground (Leweke et al., 2016). The interaction of a pair of longitudinal vortices exhibiting symmetric spatial oscillations with the ground prevents the large-scale ring vortex formation, which is generally the outcome of the Crow mechanism. However, these dynamics are not observed in the antisymmetric oscillation of the vortices in the HST wake in the first place, indicating further work is required to isolate the contribution the ground has to the unsteady characteristics observed in the results presented.

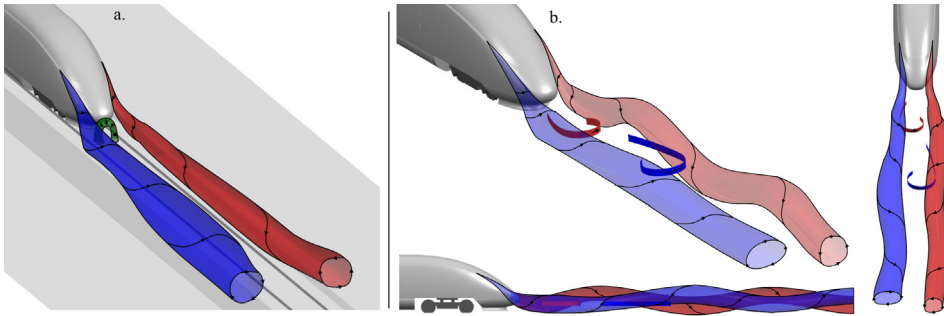


Fig. 18. (a) Time-averaged wake topology (first appeared in Bell et al. (2016)) and (b) unsteady wake topology.

4. Conclusions

The dominant three-dimensional dynamics of a pair of counter-rotating streamwise vortices that are present in the wake of a high-speed train has been presented. The model ICE3 HST investigated is typical of modern, streamlined HSTs in operation today. The insights have been provided by a 1/10th scale wind-tunnel experiment, which utilised high-frequency multi-hole dynamic pressure probes, two-dimensional total-pressure arrays and one-dimensional multi-hole arrays to investigate the near-wake unsteady wake structure.

The dominant identifiable periodic flow modification to this large-scale counter-rotating streamwise vortex pair is a spanwise oscillation of the two vortices together, resulting in an antisymmetric wake. This leads to alternating dominance, 180° out-of-phase, of each vortex. One vortex grows in size and moves upwards and outwards, while the other reduces size and moves downwards and inwards (Fig. 18b) and then vice-versa to complete the cycle. This periodic motion occurs at a frequency of $St_W = 0.2$.

The triggering of this alternating dominance of the streamwise vortices appears to be associated with vortex shedding from the sides of the train as the boundary layer advects downstream and rolls up into von Kármán-like vortices that are shed into the wake. These alternatively perturb each vortex of the trailing pair. Presumably there is also realignment of this originally vertically aligned vorticity into the streamwise direction through tilting, causing a change in the circulation of each trailing vortex with time.

Signs of both antisymmetric and symmetric perturbations were observed in the wake through Proper Orthogonal Decomposition of the total pressure data measured by a 120-probe total pressure array. The antisymmetric mode contributed significantly greater to the fluctuating total pressure (24%) than the symmetric mode (7%). This is also consistent with why the antisymmetric mode was dominant in the phase-averaging of the 4-hole probe data. However, both modes were found to exhibit the same dominant frequency of $St_W = 0.2$, and show a level of correlation with each other. This indicates that for this flow they co-exist together over the same periodic cycle. A possible explanation for the much weaker symmetric mode is the presence of periodic shedding of a vortex or hairpin-type structure off the tail tip, similar to that observed in automotive wakes. Such a structure was indicated in surface pressure and velocity profiles in the wake from the same experiment published by Bell et al. (2016).

Semi-quantitatively, the observed wavelength of the wake oscillation is consistent with the preferred wavelength of a Crow instability of a vortex pair, which is 8–9 spanwise separation distances (b), and lower for wider cores, as is the case here. The observed wavelength of the spatial oscillation of the trailing vortices here is $7.3b$.

Thus, a plausible scenario describing the development of the oscillating wake is that periodic vortex shedding occurs off the sides of the vehicle which are formed from tilting of boundary layer vorticity. The shed vortices perturb, interact and to some extent merge with the streamwise vortex pair, periodically influencing the size, location and circulation of each vortex of the pair. Counter-rotating vortices are unstable to the Crow instability, which could cause the oscillations to grow in amplitude with downstream distance. It appears that the period of shedding coupled with the convection velocity in the wake provide the right conditions to perturb the trailing vortex pair to have a wavelength close to the optimum Crow wavelength. On top of this underlying periodicity, the wake also shows considerable randomness, as might be expected in a fully turbulent, high Reynolds number flow.

Similar features, i.e., a counter-rotating vortex pair from the C-pillars and regular shedding from surfaces, have been observed in automotive wakes; however, the streamwise vortex dynamics appears different.

The alternating dominance of the pair of streamwise vortices causes the bulk slipstream velocity in the wake to exhibit spanwise oscillations in the same direction as the dominant vortex. The different stages of the fluctuation are responsible for the largest peaks in slipstream, and subsequent high levels of variation that a stationary observer would experience beyond the path of the vehicle. Peak slipstream occurs when the bulk slipstream oscillates towards the observer as the HST and its wake passes by. This periodic wake structure coincides with fluctuating pressure on the surface (Bell et al., 2016) that also has important implications for the drag and stability of the HST, as well as comfort for passengers.

The sensitivity of these findings to the experimental limitations: the reduced length of the model, the presence of a static floor and the reduced Reynolds number are yet to be quantified, and this investigation is ongoing. Despite these

experimental limitations, comparison with wake structure and dynamics in predominantly numerical literature, and the ability of the proposed flow structure to explain phenomenon established in full-scale and scaled moving-model experiments, together suggests that the findings of this work are representative of the time-averaged and unsteady wake structure and resulting slipstream around a full-scale high-speed train. This work represents a step forwards in the understanding of the unsteady wake and its effects on slipstream, insight that may be utilized for optimization and risk mitigation for the next generation of high-speed trains.

Acknowledgements

The Faculty of Engineering, Monash University, is acknowledged for the Engineering Research Living Allowance stipend scholarship for J.R. Bell. The DIN Standards Railway Committee (FSF) is acknowledged for providing the ICE3 geometry.

References

- Ahmed, S.R., 1983. Influence on base slant on the wake structure and drag of road vehicles. *J. Fluids Eng. Trans. ASME* 105 (4), 429–434.
- Baker, C., Quinn, A., Sima, M., Hoefener, L., Licciardello, R., 2012. Full scale measurement and analysis of train slipstreams and wakes: Part 1 ensemble averages. *Proc. Inst. Mech. Eng. Part F: J. Rail Rapid Transp.*
- Baker, C.J., 2010. The flow around high speed trains. *J. Wind Eng. Ind. Aerodyn.* 98, 277–298.
- Barker, S.J., Crow, S.C., 1977. The motion of two-dimensional vortex pairs in a ground effect. *J. Fluid Mech.* 82, 659–671.
- Bearman, P.W., 1997. Near wake flows behind two- and three-dimensional bluff bodies. *J. Wind Eng. Ind. Aerodyn.* 69–71, 33–54.
- Bell, J.R., Burton, D., Thompson, M.C., Herbst, A.H., Sheridan, J., 2014. Wind tunnel analysis of the slipstream and wake of a high-speed train. *J. Wind Eng. Ind. Aerodyn.* 134, 122–138.
- Bell, J.R., Burton, D., Thompson, M.C., Herbst, A.H., Sheridan, J., 2015. Moving model analysis of the slipstream and wake of a high-speed train. *J. Wind Eng. Ind. Aerodyn.* 136, 127–137.
- Bell, J.R., Burton, D., Thompson, M.C., Herbst, A.H., Sheridan, J., 2016. Flow topology and unsteady features of the wake of a high-speed train. *J. Fluids Struct.* 61, 168–183.
- Bergh, H., Tijdeman, H., 1965. Theoretical and Experimental Results for the Dynamic Response of Pressure Measuring Systems. National Aero and Astronautical Research Institute, Amsterdam, 328 (Report NLR-TRF).
- Breitsamter, C., 2011. Wake vortex characteristics of transport aircraft. *Prog. Aerosp. Sci.* 47, 89–134.
- CEN European Standard. 2009. Railway Applications—Aerodynamics Part 4: Requirements and Test Procedures for Aerodynamics on Open Track, CEN EN 14067-4.
- Chen, J., Haynes, B.S., Fletcher, D.F., 2000. Cobra probe measurements of mean velocities, Reynolds stresses and high-order velocity correlations in pipe flows. *Exp. Thermal Fluid Sci.* 21, 206–217.
- Crow, S.C., 1970. Stability theory for a pair of trailing vortices. *AIAA J.* 8 (12), 2172–2179.
- DIN Standards Committee Railway/Normenausschuss Fahrweg und Schienenfahrzeuge (FSF), 2014. (<http://www.fsf.din.de>).
- European Rail Agency (ERA). 2008. EU Technical Specification for Interoperability Relating to the 'Rolling Stock' Sub-System of the Trans-European High-Speed Rail System (HS RST TSI). 232/EC.
- Gerrard, J.H., 1966. The mechanics of the formation region of vortices behind bluff bodies. *J. Fluid Mech.* 25, 401–413.
- Gilhome, B.R., Saunders, J.W., Sheridan, J., 2001. Time Averaged and Unsteady Near-Wake Analysis of Cars. SAE Technical Paper, 01-1040.
- Graftieaux, L., Michard, M., Grosjean, N., 2001. Combining piv, pod and vortex identification algorithms for the study of unsteady turbulent swirling flows. *Meas. Sci. Technol.* 12, 1422–1429.
- Graftieaux, L., Michard, M., Grosjean, N., 2001. Combining piv, pod and vortex identification algorithms for the study of unsteady turbulent swirling flows. *Meas. Sci. Technol.* 12, 1422–1429.
- Heine, D., Lauenroth, G., Haff, J., Huntgeburth, S., Ehrenfried, K., 2013. High-speed particle image velocimetry on a moving train model. In: 2nd International Symposium on Rail Aerodynamics, Berlin, Germany.
- Hemida, H., Baker, C., Gao, G., 2014. The calculation of train slipstreams using large-eddy simulation. *Proc. Inst. Mech. Eng. Part F: J. Rail Rapid Transp.* 228 (1), 25–36.
- Hooper, J.D., Musgrove, A.R., 1997. Reynolds stress, mean velocity, and dynamic static pressure measurement by a four-hole pressure probe. *Exp. Thermal Fluid Sci.* 15, 375–383.
- Huerre, P., Monkewitz, P.A., 1990. Local and global instabilities in spatially developing flows. *Annu. Rev. Fluid Mech.* 22, 473–537.
- Iberall, A.S., 1950. Attenuation of oscillatory pressures in instrument lines. US Department of Commerce National Bureau of Standards, 45 (RP2115), 93–107.
- Irwin, H.P.A.H., Cooper, K.R., Girard, R., 1979. Correction of distortion effects caused by tubing systems in measurements of fluctuating pressures. *J. Ind. Aerodyn.* 5, 93–107.
- Jeong, J., Hussain, F., 1995. On the identification of a vortex. *J. Fluid Mech.* 285, 69–94.
- Kohri, I., Yamanashi, T., Nasu, T., Hashizume, Y., Katoh, D., Study on the Transient Behaviour of the Vortex Structure Behind Ahmed body. SAE Technical Paper, 01-0597.
- Krajnović, S., Davidson, L., 2005. Influence of floor motions in wind tunnels on the aerodynamics of road vehicles. *J. Wind Eng. Ind. Aerodyn.* 93, 677–696.
- Lödberg, O., Fransson, J.H.M., Alfredsson, P.H., 2009. Streamwise evolution of longitudinal vortices in a turbulent boundary layer. *J. Fluid Mech.* 623.
- Lewke, T., Le Dizès, S., Williamson, C.H.K., 2016. Dynamics and instabilities of vortex pairs. *Annu. Rev. Fluid Mech.* 48, 507–541.
- Lienhart, H., Pêgo, J.P., 2012. Spectral Density and Time Scales of Velocity Fluctuations in the Wake of a Simplified Car Model. SAE Technical Paper, 01-0592.
- Lumley, J.L., 1967. The structure of inhomogeneous turbulent flows. In: Yaglom, A.M., Tatarski, V.I. (Eds.), *Atmos. Turbul. Radio Wave Propag.*, pp. 166–178.
- Morel, T., 1980. Effect of base slant on flow in the near wake of an axisymmetric cylinder. *Aeronaut. Q.*, 132–147. pages.
- Muld, T., Efraimsson, G., Hennigson, D.S., 2012. Mode decomposition on surface-mounted cube. *Flow Turbul. Combust.* 88, 279–310.
- Muld, T., Efraimsson, G., Hennigson, D.S., 2012. Flow structures around a high-speed train extracted using proper orthogonal decomposition and dynamic mode decomposition. *Proc. Inst. Mech. Eng. Part F: J. Rail Rapid Transp.* 57, 87–97.
- Muld, T., Efraimsson, G., Hennigson, D.S., 2012. Mode decomposition and slipstream velocities in the wake of two high-speed trains. *Int. J. Railway Technol.*. Submitted for publication.
- Muld, T., Efraimsson, G., Hennigson, D.S., 2013. Wake characteristics of high-speed trains with different lengths. *Proc. Inst. Mech. Eng. Part F: J. Rail Rapid Transp.* Published online. <http://dx.doi.org/10.1177/0954409712473922>.
- Pauley, W.R., Eaton, J.K., 1988. Experimental study of the development of longitudinal vortex pairs embedded in a turbulent boundary layer. *AIAA J.* 26 (7), 816–823.
- Perrin, R., Braza, M., Cid, E., Cazin, S., Barthet, A., Sevrain, A., Mockett, C., Thiele, F., 2007. Obtaining phase averaged turbulence properties in the near wake of a circular cylinder at high Reynolds number using pod. *Exp. Fluids* 43, 341–355.

- Peters, J.L., 1983. Aerodynamics of very high speed trains and maglev vehicles: state of the art and future potential. *Int. J. Veh. Des. Spec. Publ. SP3*, 308–341.
- Pii, L., Vanoli, E., Polidoro, F., Gautier, S., Tabbal, A., 2014. A full scale simulation of a high speed train for slipstream prediction. In: Proceedings of the Transport Research Arena, Paris, France..
- Pope, C.W., 2007. Effective Management of Risk from Slipstream Effects at Tracksides and Platforms. Rail Safety and Standards Board—T425 Report.
- Roshko, A., 1961. Experiments on the flow past a circular cylinder at very high Reynolds number. *J. Fluid Mech.* 10, 345–356.
- Schetz, J.A., 2001. Aerodynamics of high-speed trains. *Annu. Rev. Fluid Mech.* 33, 371–414.
- Schulte-Werning, B., Heine, B., Matschke, C., 2001. Slipstream development and wake flow characteristics of modern high-speed trains. *J. Appl. Math. Mech.* 81 (S3), 789–790.
- Schulte-Werning, B., Heine, B., Matschke, C., 2003. Unsteady wake flow characteristics of high-speed trains. *Proc. Appl. Maths Mech.* 2, 332–333.
- Sims-Williams, D.B., Duncan, B., 1999. The Ahmed Model Unsteady Wake: Experimental and Computational Analyses. SAE Technical Paper, 1999-01-0809.
- Sims-Williams, D.B., Duncan, B., 2003. The Ahmed Model Unsteady Wake: Experimental and Computational Analyses. SAE Technical Paper, 2003-01-1315.
- Sims-Williams, D.B., Dominy, R.G., Howell, J.P., 2001. An Investigation into Large Scale Unsteady Structures in the Wake of Real and Idealized Hatchback Car Models. SAE Technical Paper, 2001-01-1041.
- Sims-Williams, D.B., Kaye, S., Watkins, S., 2006. Periodic Structures Within the Formation Region of the Trailing Vortices. SAE Technical Paper, 2006-01-1032.
- Sirovich, L., 1987. Turbulence and the dynamics of coherent structures. Part i: coherent structures. *Q. Appl. Math.* 45 (3), 561–590.
- Spalart, P.R., 1998. Airplane trailing vortices. *Annu. Rev. Fluid Mech.* 30, 107–138.
- Steijl, R., Hoijmakers, H.W.M., 2011. High-resolution simulations of Crow and Widnall instabilities in a vortex pair. In: 39th AIAA Aerospace Sciences Meeting and Exhibit, 8–11 January, Reno, NV..
- Strachan, R.K., Knowles, K., Lawson, N.J., 2007. The vortex structure behind an Ahmed reference model in the presence of a moving ground plane. *Exp. Fluids* 42, 659–669.
- Tombazis, N., Bearman, P.W., 1997. A study of three-dimensional aspects of vortex shedding from a bluff body with a mild geometric disturbance. *J. Fluid Mech.* 330, 85–112.
- Vino, G., Watkins, S., Mousley, P., Watmuff, J., Prasad, S., 2005. Flow structures in the near-wake of the Ahmed model. *J. Fluids Struct.* 20, 673–695.
- Wang, X.W., Zhou, Y., Pin, Y.F., Chan, T.L., 2013. Turbulent near wake of an Ahmed vehicle model. *Exp. Fluids* 54, 1490.
- Weise, M., Schober, M., Orellano, A., 2006. Slipstream velocities induced by trains. In: Proceedings of the WSEAS International Conference on Fluid Mechanics and Aerodynamics, Elounda, Greece..
- Westphal, R.V., Mehta, R.D., 1989. Interaction of an oscillating vortex with a turbulent boundary layer. *Exp. Fluids* 7, 405–411.
- Williamson, C.H.K., 1996. Vortex dynamics in the cylinder wake. *Annu. Rev. Fluid Mech.* 28, 477–539.
- Yao, S., Sun, Z., Guo, D., Chen, D., Yang, G., 2013. Numerical study on wake characteristics of high-speed trains. *Acta Mech. Sin.* 29 (6), 811–822.